Supplementary Information for

Integrated terahertz vortex beam emitter for rotating target detection

JINGYA XIE,[1] JUN QIAN,[1] TENGJIAO WANG,[1] LINJIE ZHOU,[2,*] ,

XIAOFEI ZANG,[1] LIN CHEN,[1] YIMING ZHU[1,**], AND SONGLIN

ZHUANG[1]

[1]*Terahertz Technology Innovation Research Institute, and Shanghai Key Lab of Modern*

Optical System, University of Shanghai for Science and Technology, No. 516 JunGong

Road, Shanghai, 200093, China

[2]*State Key Laboratory of Advanced Optical Communication Systems and Networks,*

Department of Electronic Engineering, Shanghai Jiao Tong University, Shanghai

200240, China;

*ljzhou@sjtu.edu.cn

**ymzhu@usst.edu.cn

Supplementary Note 1 Research on THz Vortex Beam Emitters in Recent Years

Table S1. Progress and comparison of THz vortex beam emitters in recent years

Ref.	Method	Size (mm×mm)	Principle	OAM modes	Tunability	Freq. (THz)
17	Spiral phase plate	25.4×25.4	Wavefront modulation	± 1 or ± 2	No	2 or 4
34	Spiral phase plate	20×20	Wavefront modulation	+1 and +2	No	0.62
19	Metasurface	8×8	Wavefront modulation	1, 2 and 3	No	0.75
35	Discrete Dielectric Lens	15×15	Wavefront modulation	± 1 and ± 2	Yes	0.3
36	Achromatic polarization elements	/	Wavefront modulation	± 1	Yes	0.75-2

21	q-plate	8×8	Wavefront modulation	1 and 4	No	1
20	q-plate	40×40	Wavefront modulation	1/2	No	0.15
22	Hologram	15×15	Wavefront modulation	1, 2 and 3	Yes	1
23	Hologram	600×600	Wavefront modulation	+1	No	0.31
37	Binary Phase Plate	38×38	Wavefront modulation	± 1 and ± 2	No	2.1
38	Binary Phase Plate	30×30	Wavefront modulation	± 1 and ± 2	No	2.1
39	THz liquid crystal forked polarization grating	15×20	Wavefront modulation	± 1	No	1
This Work	WGM	15×15	Waveguide Excitation	± 1, ± 2 and ± 3	Yes	0.17-0.19

Supplementary Note 2 Interaction of transverse spin and OAM

The evanescent waves in strong confinement ring waveguides exhibit a local longitudinal electric field component ($\mathbf{E}_\varphi$) that is in quadrature phase with the radial component ($\mathbf{E}_r$) [40]. These waves possess a circular polarization state with the z-direction serving as their rotation axis, giving rise to local spin angular momentum (SAM) that is orthogonal to the local propagation direction ($+\varphi$ or $-\varphi$) of the whispering gallery modes (WGM). As a result, the local SAM in the evanescent field produces a transverse spin.

The sub-wavelength grating scatterers used in the device are of a small rectangular parallelepiped shape (with dimensions $a \times b \times c$), which orientation are parallel to the local coordinates (r, φ, z). The light scattered from each grating element can be approximated by radiation from a dipole antenna, with the phase locked to the driving transverse evanescent fields [41]. Assuming that the dipole antenna carries the defined moment $\mathbf{p}$, the concept of particle

polarizability α is used to describe the relationship between the external field $\mathbf{E}$ and $\mathbf{p}$ [41]

$$\mathbf{p} = \alpha\mathbf{E} \tag{S1}$$

where the polarizability α is generally a tensor. If the external field is oriented along the local coordinate axis (r, φ, z) on the sides of scatterers, then α can be expressed as a matrix which the diagonal component equal α_{ii} ($i = r$, φ, z) and other components equal zero [42]

$$\alpha = \begin{bmatrix} \alpha_{rr} & 0 & 0 \\ 0 & \alpha_{\varphi\varphi} & 0 \\ 0 & 0 & \alpha_{zz} \end{bmatrix} \tag{S2}$$

Note that high-resistance silicon has almost no loss in the THz frequency band. Hence, we can neglect the absorption loss of the high-resistance silicon scatterers, that is, α_{ii} is a real number which quantify the scatterer modulation on the strength of the electric components $\mathbf{E}_i$. Therefore, according to the above Equation (S1) and (S2), the local evanescent wave of each scatterer can be described as

$$\begin{bmatrix} \mathbf{p}_r \\ \mathbf{p}_\varphi \\ \mathbf{p}_z \end{bmatrix} = \begin{bmatrix} \alpha_{rr} & 0 & 0 \\ 0 & \alpha_{\varphi\varphi} & 0 \\ 0 & 0 & \alpha_{zz} \end{bmatrix} \begin{bmatrix} \mathbf{E}_r \\ \mathbf{E}_\varphi \\ \mathbf{E}_z \end{bmatrix}, \text{ or, } \begin{cases} \mathbf{p}_r = \alpha_{rr}\mathbf{E}_r \\ \mathbf{p}_\varphi = \alpha_{\varphi\varphi}\mathbf{E}_\varphi \\ \mathbf{p}_z = \alpha_{zz}\mathbf{E}_z \end{cases} \quad (S3)$$

According to the Equation (S3), the transverse components ($\mathbf{p}_r$ and $\mathbf{p}_\varphi$) on the radiation field have no instantaneous phase shift, thus always maintain $\pm\pi/2$ phase difference with each other.

The local transverse spin state within the evanescent wave can be defined as

$$\sigma = \frac{|\mathbf{p}_L|^2 - |\mathbf{p}_R|^2}{|\mathbf{p}_L|^2 + |\mathbf{p}_R|^2} \quad (S4)$$

$\mathbf{p}_L$ and $\mathbf{p}_R$ represent the local left- and right-hand circular components in the evanescent wave, respectively. And they can be expressed using $\mathbf{p}_r$ and $\mathbf{p}_\varphi$, which are determined under the cylindrical coordinate system. Specifically, if κ is defined as the ratio of the two components of the radiation field, i.e., $\kappa = i\mathbf{p}_\varphi/\mathbf{p}_r$, then the local transverse spin σ can be given by[33]:

$$\sigma = -\frac{2\kappa}{1+\kappa^2} \quad (S5)$$

Therefore, the ratio between the longitudinal and radial electric field components within the evanescent waves ($i\mathbf{E}_\varphi/\mathbf{E}_r$) plays a crucial role in influencing the transverse spin state. This ratio significantly affects the value of κ, which, in turn, impacts the value of σ.

In the cylindrical coordinate system, the WGM's evanescent wave can be expressed as $\mathbf{E}_{in} \propto e^{\pm ip\varphi}[\mathbf{E}_r \ \mathbf{E}_\varphi]^T$, with p denoting the number of optical periods surrounding the resonator. Two counter-propagating WGMs (CCW and CW), with an azimuthal mode number of p (CCW) and $-p$ (CW), respectively, exist at the same wavelength. Calculated by the transfer matrix method, the connection between the output cylindrical vector vortex (CVV) and the transverse spin state σ is given by[33]

$$\mathbf{E}_{\text{out}} \propto \frac{1}{2}\left\{\sqrt{1+\sigma}e^{i(l_{TC}-1)\varphi}\begin{bmatrix}1\\i\end{bmatrix} + \sqrt{1-\sigma}e^{i(l_{TC}+1)\varphi}\begin{bmatrix}1\\-i\end{bmatrix}\right\} \qquad (S6)$$

The topological charge, l_{TC}, is determined by the equation $l_{TC} = \pm(p - q)$. Here, the Jones vector is expressed in the global
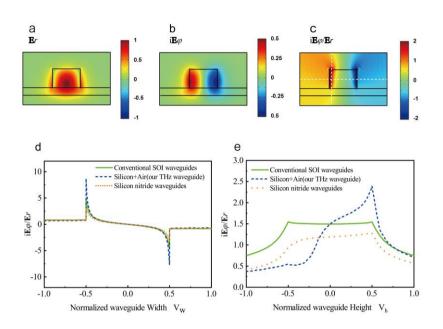
reference frame using the x- and y-polarization basis (i.e., $[\mathbf{E}_x\ \mathbf{E}_y]^T$).

Additionally, the topological charge of left-hand circular polarization (LHCP) and right-hand circular polarization (RHCP) vortices in Equation (S6) is $l_{TC}-1$ and $l_{TC}+1$, respectively. The CVVs carry an OAM component that is subject to the transverse-spin state of the WGM evanescent wave. It should be noted that the quasi-TE mode injected from diverse ports of the bus waveguide can also bring about a flip of the transverse-spin state. If we assume that the transverse-spin state of the SAM generated by excitation from port 1 in Fig. 1(a) is σ, then the excitation from port 2 will generate the SAM carrying the transverse-spin state of $-\sigma$.

Supplementary Note 3 Discussion on the electric component ratio

The magnitude of the electric component ratio $i\mathbf{E}_\varphi/\mathbf{E}_r$ is a critical factor for our vortex emitter, as it is directly related to the ratio of the two electric components of the radiation field κ. To investigate the $i\mathbf{E}_\varphi/\mathbf{E}_r$ ratio around the waveguide, we conducted numerical simulations of the cross-sectional electric field distribution of the fundamental TE waveguide modes. Our THz device employs ridge-type silicon waveguides to achieve strong confinement, with a ridge width of 500 μm, a ridge height of 340 μm, and a slab thickness of 130 μm. The high-resistivity Si boasts a dielectric constant of $\varepsilon_r = 11.7$ and a resistivity exceeding 20 kΩ·cm. The effective refractive index of the TE mode is calculated to be $n_{eff} = 2.78$ at 180 GHz. The distribution of the strong azimuthal component $\mathbf{E}_\varphi$ is predominantly centered within the waveguide, whereas $\mathbf{E}_r$, which is phase-shifted by $\pm\pi/2$ relative to $\mathbf{E}_\varphi$, is located at the lateral core-cladding interface

(i.e. sidewalls), as depicted in Fig. S1(a) and S1(b). The component ratio $i\mathbf{E}_\varphi/\mathbf{E}_r$ is illustrated in Fig. S1(c). Beyond the waveguide sidewalls, this ratio remains nearly constant within the decaying evanescent wave, given that both components decay at the same rate. Figure S1(d) illustrates the one-dimensional plot of $i\mathbf{E}_\varphi/\mathbf{E}_r$ at the location corresponding to the white horizontal line in Fig. S1(c). To provide a comparison with conventional waveguides, the results of silicon-on-insulator (SOI) waveguides and silicon nitride waveguides in the optical domain ($\lambda = 1.55$ μm) are also presented. The simulation employed SOI waveguides with a width of 500 nm and a thickness of 220 nm, as well as a silicon nitride waveguide with dimensions of 0.8 μm in width and 0.6 μm in height, which was surrounded by air and positioned on a SiO_2 substrate. The results demonstrate that a high refractive index contrast has a substantial impact on the magnitude of the $i\mathbf{E}_\varphi/\mathbf{E}_r$ ratio, particularly in the vicinity of the waveguide sidewalls. In contrast, the impact of

refractive index contrast on the $i\mathbf{E}_\varphi/\mathbf{E}_r$ ratio at the core-cladding interface at the top of the waveguide is relatively smaller. This is evidenced by the results presented in Fig. S1(e), where the $i\mathbf{E}_\varphi/\mathbf{E}_r$ at the location corresponds to the white vertical line in Fig. S1(c). Hence, etching a grating on the top of the THz silicon waveguides has the potential to allow for fine-tuning of the grating scatterers, which could enable the transverse spin angular momentum to approach ± 1. Consequently, this can facilitate the production of a single circularly polarized OAM beam.

Fig. S1 a-c displays the field component distributions of the quasi-TE mode in a high-resistance Si waveguide at 180 GHz. Specifically, it presents: **a** the cross-sectional field distribution of the radial component E_r, **b** the cross-sectional field distribution of the azimuthal component iE_φ, where i is the imaginary unit, and **c** the distribution of the component ratio iE_φ/E_r over the waveguide cross section and the evanescent region. **d** The one-dimensional curve of iE_φ/E_r is shown at the location corresponding to the white horizontal line in **Fig. S1c**, including our THz waveguide, conventional SOI waveguides, and silicon nitride

waveguides in the optical domain (λ = 1.55 μm). **e** The one-dimensional curve of

$i\mathbf{E}_{\varphi}/\mathbf{E}_r$ is plotted at the location corresponding to the white vertical line in **Fig. S1c**,

including our THz waveguide, conventional SOI waveguides, and silicon nitride

waveguides in the optical domain (λ = 1.55 μm).

Supplementary Note 4 The characteristics of non-scalar vortex beams (i.e. traditional vector vortex beam) generated by a WGM resonator-based emitter

Traditional vortex emitters based on WGM resonators use side-wall etched gratings on the ring waveguide, which emit a CVV beam consisting of both LHCP and RHCP components, as described in Equation S6. Here, our research aims to compare the effect of suppressing one circular polarization component in the device. In Figure S2, the radiation cross-sectional field distributions for the x- and y-polarizations of the WGM resonator-based vortex emitter with a side-wall-etched grating are presented based on the simulation results. The grating employed in this study features a duty cycle of 0.5. Along with this, the microring waveguide has a width of 450 μm, while the bus waveguide is 500 μm wide with a gap of 50 μm. The remaining parameters correspond to the

optimized scalar vortex THz device presented in this paper. The topological charge of the OAM l_{TC} takes values of 0, 1, and 2, corresponding to the results shown in Fig. 3. It is evident that on the phase distributions of the x- and y-polarizations, multiple singularities appear. Furthermore, the intensity distribution of the electric field noticeably deviates from the ideal distribution of a vortex beam (which typically consists of a ring of intensity with a null at the center). Fig. S3 reveals the electric field intensity and phase distribution of the output CVV beam, separated into the LHCP and RHCP components. It is evident that both components have high energy, resulting in the electric field on the x- and y-polarizations no longer having the typical characteristics of a conventional vortex beam. As a consequence, these vector vortex beams cannot be directly detected and received by linearly polarized antennas, thus limiting their practical applications.
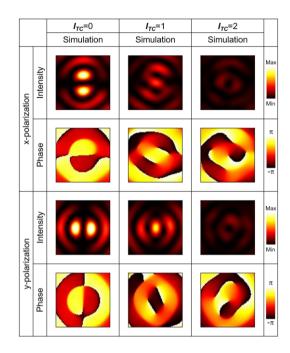
Fig. S2 Simulated radiation-cross-sectional field distributions of the *x*- and

y-polarization components for the traditional OAM emitters with side-wall etched

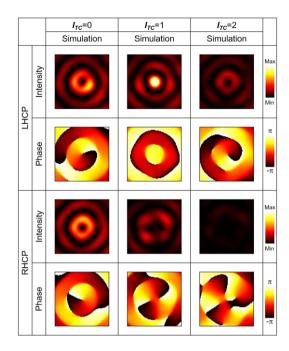gratings. l_{TC} is the topological charge.

Fig. S3 Simulated radiation-cross-sectional field distributions of the left-hand circular and right-hand circular polarization components for the traditional OAM emitters with side-wall etched gratings. l_{TC} is the topological charge.